

## Karhunen–Loeve representations of turbulent channel flows using the method of snapshots<sup>¶</sup>

R. A. Handler<sup>1,\*</sup>,<sup>†</sup>, K. D. Housiadas<sup>2,‡</sup> and A. N. Beris<sup>3,§</sup>

<sup>1</sup>*Naval Research Laboratory, Washington, DC 20375, U.S.A.*

<sup>2</sup>*Department of Mathematics, University of the Aegean, Samos, Greece*

<sup>3</sup>*Department of Chemical Engineering, University of Delaware, Newark, DE 19716, U.S.A.*

### SUMMARY

For three-dimensional flows with one inhomogeneous spatial coordinate and two periodic directions, the Karhunen–Loeve procedure is typically formulated as a spatial eigenvalue problem. This is normally referred to as the direct method (DM). Here we derive an equivalent formulation in which the eigenvalue problem is formulated in the temporal coordinate. It is shown that this so-called method of snapshots (MOS) has some numerical advantages when compared to the DM. In particular, the MOS can be formulated purely as a matrix composed of scalars, thus avoiding the need to construct a matrix of matrices as in the DM. In addition, the MOS avoids the need for so-called weight functions, which emerge in the DM as a result of the non-uniform grid typically employed in the inhomogeneous direction. The avoidance of such weight functions, which may exhibit singular behaviour, guarantees satisfaction of the boundary conditions. The MOS is applied to data sets recently obtained from the direct simulation of turbulence in a channel in which viscoelasticity is imparted to the fluid using a Giesekus model. The analysis reveals a steep drop in the dimensionality of the turbulence as viscoelasticity is increased. This is consistent with the results that have been obtained with other viscoelastic models, thus revealing an essential generic feature of polymer-induced drag reduced turbulent flows. Published in 2006 by John Wiley & Sons, Ltd.

KEY WORDS: Karhunen–Loeve; turbulence; drag reduction; viscoelasticity

\*Correspondence to: R. A. Handler, Naval Research Laboratory, Remote Sensing Division, 4555 Overlook Ave. SW, Washington, DC 20375, U.S.A.

<sup>†</sup>E-mail: robert.handler@nrl.navy.mil

<sup>‡</sup>E-mail: housiadas@che.udel.edu

<sup>§</sup>E-mail: beris@che.udel.edu

<sup>¶</sup>This article is a U.S. Government work and is in the public domain in the U.S.A.

Contract/grant sponsor: DARPA; contract/grant number: MDA972-01-1-0007

Contract/grant sponsor: NCSA; contract/grant number: MCA96N005P

*Received 15 December 2005*

*Revised 1 March 2006*

*Accepted 1 March 2006*

## 1. INTRODUCTION

The Karhunen–Loeve method (KL) of analysis has been applied extensively to complex data sets in a wide variety of fields. It has been found particularly useful in meteorology and oceanography [1] where it is referred to as principal component analysis, but has also been used more recently in the analysis of complex three-dimensional turbulent flows. In the case of turbulence, the KL method has been used to explore the nature of coherent structures embedded in seemingly chaotic flows [2–5]. It has also found use in the development of low-order dynamical system models [6–8] for these flows and in exploring non-linear energy dynamics [9].

Channel flow turbulence (i.e. flow between two parallel plates driven by a constant pressure gradient) has undergone intense study in recent years since it has been interpreted as a model for more complex wall-bounded turbulent boundary layer flows. The simplicity of the channel geometry allows for direct numerical simulations (DNS), resulting in the creation of very large data sets which require interrogation. The standard formulation of the KL method for these flows [10], often referred to as the direct method (DM), involves an eigenvalue decomposition of the Reynolds stress correlation matrix. Indeed, this approach has been used exclusively to date to solve problems of the channel flow type. However, as pointed out by Sirovich and Kirby [11], an alternative approach called the method of snapshots (MOS) has some advantages in circumstances where the direct approach is computationally infeasible. In this paper, we formulate the MOS for the case of channel flow and demonstrate that, although the DM is generally tractable in this circumstance, the MOS affords several useful computational advantages which will be described in detail below. The MOS was then applied to the case of the fully developed turbulent flow of a viscoelastic fluid. The data sets used for the analysis were obtained from a series of direct numerical simulations in which a Giesekus model of viscoelasticity was employed. It is shown clearly that viscoelasticity profoundly reduces the dimensionality of the turbulence. This finding corroborates earlier work [12, 13] using a different viscoelastic model, the finite-extensibility non-linear extensible with the Peterlin approximation dumbbell (FENE-P), which is a standard model for dilute polymer solutions [14], the Giesekus model being a better model for semi-dilute and concentrated systems [14, 15]. This result provides further evidence of the importance of large coherent structures in these drag reduced flows and motivates further work on applying the KL method to these cases, including possibly the development of reduced dimensionality models for viscoelastic turbulence.

## 2. FORMULATION OF THE KARHUNEN–LOEVE PROBLEM FOR A THREE-DIMENSIONAL FLOW

### 2.1. *The direct method*

For purposes of completeness, here we repeat the formulation of the DM for three-dimensional flow in a channel with two periodic directions and one inhomogeneous direction. We note, however, that these techniques can easily be extended to cases of two or three inhomogeneous directions. In the case of interest here, the velocity field is given by  $u_j(x_1, x_2, x_3, t)$ ,  $j = 1, 2, 3$ . Here, the subscripts 1 and 3 designate the homogeneous directions which, for channel flow,

are the streamwise (i.e. the direction in which the driving pressure gradient is applied) and spanwise directions, respectively, the subscript 2 designates the vertical, or wall-normal coordinate, and  $t$  is time. We may alternately use the notation  $x$ ,  $y$ , and  $z$  for the streamwise, spanwise, and wall-normal coordinates, respectively, and  $u$ ,  $v$ , and  $w$  for the streamwise, wall-normal, and spanwise velocity components. The velocity field can then be represented [16] as

$$u_j(x, y, z, t) = \sum_{n=-N/2}^{N/2-1} \sum_{m=-M/2}^{M/2-1} U_j^{nm}(y, t) e^{ik_n x} e^{ik_m z} \tag{1}$$

where  $k_n = 2\pi n/L_x$  and  $k_m = 2\pi m/L_z$  are the wavenumbers in the streamwise and spanwise directions, respectively,  $L_x$  and  $L_z$  are the streamwise and spanwise domain lengths,  $i = \sqrt{-1}$ , and  $U_j^{nm}(y, t)$  are the Fourier coefficients given by

$$U_j^{nm}(y, t) = \frac{1}{L_x L_z} \int_{-L_x/2}^{L_x/2} \int_{-L_z/2}^{L_z/2} u_j(x, y, z, t) e^{-ik_n x} e^{-ik_m z} dx dz \tag{2}$$

The flows considered here are incompressible:

$$\frac{\partial u_j}{\partial x_j} = 0 \tag{3}$$

and satisfy no-slip boundary conditions:

$$u_j(x, L_y/2, z) = u_j(x, -L_y/2, z) = 0, \quad j = 1, 2, 3 \tag{4}$$

where  $L_y$  is the domain length in the vertical direction. In (3) and in all subsequent expressions, a summation is implied on the repeated index  $j$  but never on any other repeated index unless otherwise stated.

It should be noted that other boundary conditions are of interest such as the so-called flat free surface condition:

$$\frac{\partial u}{\partial y} = \frac{\partial w}{\partial y} = v = 0 \tag{5}$$

applied on  $y = L_y$  [17–20]. Other conditions can be used such as those associated with a surfactant covered boundary [21–23], or the more general interfacial conditions between two fluid media [24]. If properly formulated, the KL procedure must preserve incompressibility and any boundary conditions such as those mentioned above.

The objective of the procedure is to find functions  $\Psi_j^{nmq}(y)$  which maximize the quantity:

$$\lambda^{nmq} = \left\langle \left| \frac{1}{L_y} \int_{-L_y/2}^{L_y/2} U_j^{nm}(y, t) \overline{\Psi_j^{nmq}}(y) dy \right|^2 \right\rangle \tag{6}$$

subject to the constraint:

$$\frac{1}{L_y} \int_{-L_y/2}^{L_y/2} \Psi_j^{nmq}(y) \overline{\Psi_j^{nmq'}}(y) dy = \delta_{qq'} \tag{7}$$

where  $\langle \dots \rangle = \frac{1}{T} \int_0^T (\dots) dt$ ,  $T$  is a suitably long time interval over which averages are taken, and conjugation is designated by an overbar. The integer index  $q$ , the so-called quantum

index, is introduced in anticipation of an eigenvalue problem which gives rise to a spectrum of eigenfunctions for each wavenumber index pair  $(n, m)$ . The eigenfunctions  $\Psi_j^{nmq}$ , and eigenvalues  $\lambda^{nmq}$ , are solutions to the integral equation [25]:

$$\frac{1}{L_y} \int_{-L_y/2}^{L_y/2} R_{ij}^{nm}(y, y') \Psi_j^{nmq}(y') \, dy' = \lambda^{nmq} \Psi_i^{nmq}(y) \quad (8)$$

where the Reynolds stress tensor is given by

$$R_{ij}^{nm}(y, y') = \langle U_i^{nm}(y, t) \overline{U_j^{nm}}(y', t) \rangle \quad (9)$$

It can then be shown that the eigenvalues are real and positive, that the eigenfunctions satisfy incompressibility:

$$\frac{\partial \Psi_j^{nmq}}{\partial x_j} = 0 \quad (10)$$

and that the eigenfunctions satisfy the boundary conditions, which for no-slip boundaries are

$$\Psi_j^{nmq}(L_y/2) = \Psi_j^{nmq}(-L_y/2) = 0 \quad (11)$$

The original Fourier coefficients can then be represented optimally as defined by (6) so that

$$U_j^{nm}(y, t) = \sum_q a^{nmq}(t) \Psi_j^{nmq}(y) \quad (12)$$

Substitution of (12) into (1) then gives an optimal representation of the three-dimensional velocity field. It should be noted that the KL eigenfunctions reduce to sinusoids in the flow directions exhibiting statistical homogeneity [10]. It follows that for channel flow, the Fourier representation given by (1) is the appropriate one in the  $x$  and  $z$  directions.

## 2.2. The method of snapshots for three-dimensional flows

An alternative procedure called the MOS is derived by changing the order of integration in (8) and (9) to give

$$\left\langle U_i^{nm}(y, t) \frac{1}{L_y} \int_{-L_y/2}^{L_y/2} \overline{U_j^{nm}}(y', t) \Psi_j^{nmq}(y') \, dy' \right\rangle = \lambda^{nmq} \Psi_i^{nmq}(y) \quad (13)$$

We then define the coefficients  $a^{nmq}$  by

$$a^{nmq}(t) = \frac{1}{L_y} \int_{-L_y/2}^{L_y/2} \overline{U_j^{nm}}(y', t) \Psi_j^{nmq}(y') \, dy' \quad (14)$$

so that the eigenfunctions are given by

$$\Psi_i^{nmq}(y) = \frac{1}{\lambda^{nmq}} \langle a^{nmq}(t) U_i^{nm}(y, t) \rangle \quad (15)$$

Changing  $i$  to  $j$ ,  $y$  to  $y'$ , and  $t$  to  $t'$  in (15) and substituting this back into (14) gives

$$\langle C^{nm}(t, t') a^{nmq}(t') \rangle_{t'} = \lambda^{nmq} a^{nmq}(t) \quad (16)$$

where

$$C^{nm}(t, t') = \frac{1}{L_y} \int_{-L_y/2}^{L_y/2} U_j^{nm}(y', t') \overline{U_j^{nm}}(y', t) dy' \tag{17}$$

and  $\langle \dots \rangle_{t'}$  indicates integration over  $t'$  and division by  $T$ . Finally, it can easily be shown that requiring the spatial eigenfunctions to be orthonormal as defined by (7) is equivalent to requiring the time-dependent eigenfunctions,  $a^{nmq}$ , to obey

$$\langle a^{nmq}(t) \overline{a^{nmq'}}(t) \rangle = \lambda^{nmq} \delta_{qq'} \tag{18}$$

When the constraint given by (18) is imposed, the MOS is exactly equivalent to the DM.

### 2.3. Summary

It is useful to give a brief summary of these two formulations. In the so-called DM we form a spatial correlation matrix  $R_{ij}^{nm}(y, y')$  whose associated spatial eigenfunctions,  $\Psi_j^{nmq}(y)$ , are solved for directly by means of (8). On the other hand, in the MOS, the spatial eigenfunctions are determined indirectly by first determining temporal eigenfunctions,  $a^{nmq}$ , via (16). The spatial eigenfunctions are then determined as a weighted sum of the original data (the snapshots) as in (15), hence the name *method of snapshots*. It is also important to note that while the DM requires the construction of a *matrix of matrices* ( $R_{ij}^{nm}$ ) the MOS has inherently scalar components, since it is clear that we form the dot product  $U_j^{nm} \overline{U_j^{nm}}$  in (17). We point out the implications of this below.

Merely for purposes of consistency with the direct problem, we redefine the MOS as follows:

$$\langle \overline{C^{nm}(t, t')} b^{nmq}(t') \rangle_{t'} = \lambda^{nmq} b^{nmq}(t) \tag{19}$$

so that  $b^{nmq} = \overline{a^{nmq}}$ . With this definition of the MOS, integration over  $t'$  is associated with the variable  $\overline{U_j^{nm}}(y, t')$ , which is analogous to the DM where integration over  $y'$  is associated with the variable  $\overline{U_j^{nm}}(y', t)$ . Then the spatial eigenfunctions are obtained from

$$\Psi_j^{nmq}(y) = \frac{1}{\lambda^{nmq}} \langle \overline{b^{nmq}(t)} U_j^{nm}(y, t) \rangle \tag{20}$$

### 2.4. The discrete problem

In formulating a discrete system for the integral equations derived above, we note that in general, non-uniform grids are used in the wall-normal ( $y$ ) direction. In our codes, since we use Chebyshev polynomials ( $T_p(y/\varepsilon)$ ) to represent the velocity field in this direction, optimal grid locations in the vertical direction are given by  $y_l = \varepsilon \cos(\theta_l)$ ,  $l = 0, \dots, L$ , where  $\varepsilon = L_y/2$ , and  $\theta_l = \pi l/L$ . This choice for  $\varepsilon$  yields the desired range ( $-1 \leq y/\varepsilon \leq 1$ ) for the argument of the Chebyshev polynomials.

To form the discrete problem for the DM we first apply the transformation  $y = \varepsilon \cos(\theta)$  to (8). In addition, to preserve the Hermitian nature of the kernel we introduce weights given by

$$w(\theta) = \sqrt{\sin(\theta)/2} \tag{21}$$

The resultant problem then becomes

$$\int_0^\pi [w(\theta)R_{ij}^{nm}(\theta, \theta')w(\theta')] \Psi_j^{nmq}(\theta')w(\theta') d\theta' = \lambda^{nmq} \Psi_i^{nmq}(\theta)w(\theta) \tag{22}$$

with the constraint

$$\int_0^\pi \Psi_j^{nmq}(\theta) \overline{\Psi_j^{nmq'}}(\theta)w^2(\theta) d\theta = \delta_{qq'} \tag{23}$$

where we use the simplified notation  $R_{ij}^{nm}(\theta, \theta') \equiv R_{ij}^{nm}(\varepsilon \cos(\theta), \varepsilon \cos(\theta'))$ , and  $\Psi_i^{nmq}(\theta) \equiv \Psi_i^{nmq}(\varepsilon \cos(\theta))$ . The discrete problem then becomes

$$\sum_{l'=0}^L K_{ij}^{nm}(l, l') \Phi_j^{nmq}(l') \Delta\theta = \lambda^{nmq} \Phi_i^{nmq}(l) \tag{24}$$

with the constraint

$$\sum_{l'=0}^L \Phi_j^{nmq}(l) \overline{\Phi_j^{nmq'}}(l) = \delta_{qq'} \tag{25}$$

where  $\Delta\theta = \pi/L$ .

Here we have used the simplified notation  $K_{ij}^{nm}(l, l') \equiv K_{ij}^{nm}(\varepsilon \cos(\theta_l), \varepsilon \cos(\theta_{l'}))$ ,  $\Phi_j^{nmq}(l) \equiv \Phi_j^{nmq}(\varepsilon \cos(\theta_l))$ , and  $w(l) \equiv w(\theta_l)$ , so that

$$K_{ij}^{nm}(l, l') = w(l)R_{ij}^{nm}(l, l')w(l') \tag{26}$$

and

$$\Phi_j^{nmq}(l) = \Psi_j^{nmq}(l)w(l)\sqrt{\Delta\theta} \tag{27}$$

The desired incompressible eigenfunctions ( $\Psi_j^{nmq}$ ) can then be obtained using (27) by dividing the auxiliary eigenfunctions ( $\Phi_j^{nmq}$ ) by the weight function. As we note below, this can lead to issues with respect to the enforcement of the boundary conditions, other than those of the no-slip type, since division by the weight functions becomes undefined at the boundaries.

In many cases, the flow may have particular symmetries which may be used to increase the sample size. In the case of channel flow, the total number of realizations can be increased by a factor of four by using the well-known symmetries of the flow. The full set of flow realizations including symmetries are given by (see Reference [10])

$$\begin{aligned} u_j^0 &\equiv (u(x, y, z, t), v(x, y, z, t), w(x, y, z, t)) \\ u_j^1 &\equiv (u(x, -y, z, t), -v(x, -y, z, t), w(x, -y, z, t)) \\ u_j^2 &\equiv (u(x, y, -z, t), v(x, y, -z, t), -w(x, y, -z, t)) \\ u_j^3 &\equiv (u(x, -y, -z, t), -v(x, -y, -z, t), -w(x, -y, -z, t)) \end{aligned} \tag{28}$$

The corresponding Fourier transforms of the above four flows are then defined as  $U_i^{nms}(y, t)$ ,  $s = 0, 1, 2, 3$ . These flows can then be used to form a new spatial correlation matrix

given by

$$R_{ij}^{nm}(y, y') = \left\langle \frac{1}{N_{\text{sym}} + 1} \sum_{s=0}^{N_{\text{sym}}} U_i^{nms}(y, t) \overline{U_j^{nms}(y', t)} \right\rangle \tag{29}$$

where  $N_{\text{sym}}$ , the number of flow symmetries, is three for channel flow.

The MOS can be discretized by first computing the complex conjugate of the integrand in (17) as follows:

$$Q^{nm}(y, t, t') = U_j^{nm}(y, t) \overline{U_j^{nm}(y, t')} \tag{30}$$

If the velocity field is expressed as a sum of Chebyshev polynomials,  $T_p$ , it is natural also to expand the integrand as

$$Q^{nm}(y, t, t') = \sum_{p=0}^P q_p^{nm}(t, t') T_p(y/\varepsilon) \tag{31}$$

The temporal correlation matrix can then be computed exactly as follows:

$$\overline{C^{nm}(t, t')} = \frac{1}{L_y} \int_{-L_y/2}^{L_y/2} \sum_{p=0}^P q_p^{nm}(t, t') T_p(y/\varepsilon) dy \tag{32}$$

By changing variables of integration ( $\bar{y} = y/\varepsilon$ ) and noting that  $\int_{-1}^1 T_p(\bar{y}) d\bar{y} = 2/(1 - p^2)$  for even values of  $p$ , (32) becomes

$$\overline{C^{nm}(t, t')} = \sum_{\substack{p=0 \\ p \text{ even}}}^P \frac{q_p^{nm}(t, t')}{1 - p^2} \tag{33}$$

Thus, once the Chebyshev coefficients of  $q_p^{nm}$  are computed (which can be performed efficiently using fast Fourier transform methods [16]),  $\overline{C^{nm}}$  can be computed using (33). The discrete form of the integral equation given by (19) can now be expressed as:

$$\frac{1}{N_r} \sum_{s'=0}^{N_r-1} \overline{C^{nm}(t_s, t_{s'})} \alpha^{nmq}(t_{s'}) = \lambda^{nmq} \alpha^{nmq}(t_s) \tag{34}$$

where we have converted the time integral in (19) to a sum over a sequence of  $N_r$  flow realizations (snapshots) obtained at equally spaced time intervals. Since we may wish to add flow symmetries to the ensemble of flow realizations as described by (28), we define  $N_r$  as the total number of available realizations including flow symmetries so that  $N_r = M_{\text{flow}} \times (N_{\text{sym}} + 1)$  where  $M_{\text{flow}}$  is the number of realizations of the flow available without employing symmetries (e.g.  $u_j^0$  in (28)). Alternatively, the summation in (34) can be interpreted as an expectation over a number of realizations preferably taken over time intervals,  $\Delta t$ , such that the time between realizations  $\Delta t \gg T_{\text{eddy}}$  where  $T_{\text{eddy}}$  is a typical large eddy turnover time for the particular turbulent flow under consideration.

Regardless of whether the DM or the MOS is used, the number of non-trivial eigenvalues and eigenfunctions will be the lesser of  $3 \times N_{\text{grid}}$  or  $M_{\text{flow}} \times (N_{\text{sym}} + 1)$  per wavenumber index pair  $(n, m)$ , where  $N_{\text{grid}}$  is the number of grid nodes in  $y$ , and the factor of three applies in the case of the three-dimensional flows under consideration here. Therefore, as pointed out

by Sirovich and Kirby [11], in cases where the number of grid nodes (or pixels) is very large compared with the number of snapshots, the MOS may be the only method that is computationally feasible. We note that these estimates regarding the number of non-trivial modes may be reduced due to the imposition of the incompressibility constraint.

2.5. *Scaling of the eigenfunctions, and the addition of symmetries in the MOS*

The eigenvectors  $\alpha^{nmq}(t_s)$ , defined by (34), returned by standard solvers such as those in EISPACK will then be orthonormal in the sense that:

$$\sum_{s=0}^{N_r-1} \alpha^{nmq}(t_s) \overline{\alpha^{nmq'}}(t_s) = \delta_{qq'} \tag{35}$$

but in order to generate spatial eigenfunctions,  $\Psi_j^{nmq}$ , as defined in (7), we need eigenvectors  $\beta^{nmq}$  such that

$$\frac{1}{N_r} \sum_{s=0}^{N_r-1} \beta^{nmq}(t_s) \overline{\beta^{nmq'}}(t_s) = \lambda^{nmq} \delta_{qq'} \tag{36}$$

Therefore, we choose

$$\beta^{nmq}(t_s) = \alpha^{nmq}(t_s) \sqrt{N_r \lambda^{nmq}} \tag{37}$$

so that the eigenfunctions given by

$$\Psi_j^{nmq}(y) = \frac{1}{\sqrt{\lambda^{nmq} N_r}} \sum_{s=0}^{N_r-1} \alpha^{nmq}(t_s) U_j^{nm}(t_s, y) \tag{38}$$

are orthonormal as defined by (7).

It is evident from the detailed description of the discrete problems described above that the MOS formulation affords some advantages as compared to the DM. First, the correlation matrix  $C^{nm}$  has purely scalar components compared to the tensor nature of  $R_{ij}$  needed for the DM. More importantly, the weight functions, which are required in the DM, are completely avoided in the MOS. These facts have two main consequences: (1) The construction of  $C^{nm}$  does not require the assembly of a matrix of matrices as in the DM, and (2) In the MOS no issues arise with regard to the singularity of the weight functions at the boundaries. In the MOS, since weights are entirely avoided in the construction of  $C^{nm}$ , any boundary conditions such as those enumerated in Section 2 (not just no-slip) will be automatically preserved. This is true by virtue of (38), which shows that the eigenfunctions are simply linearly weighted sums of the individual flows.

As alluded to above, it is straightforward to incorporate flow symmetries into the MOS. This proceeds by simply substituting for the field  $U_j^{nm}$ , the field  $V_j^{nm}$  in the computation of  $C^{nm}$ , where  $V_j^{nm}$  is defined as

$$V_j^{nm} = \begin{cases} U_j^{nm0}(y, t_k), & k = 0, 1, \dots, M_{\text{flow}} - 1 \\ U_j^{nm1}(y, t_k), & k = M_{\text{flow}} \dots 2 \times M_{\text{flow}} - 1 \\ U_j^{nm2}(y, t_k), & k = 2 \times M_{\text{flow}} \dots 3 \times M_{\text{flow}} - 1 \\ U_j^{nm3}(y, t_k), & k = 3 \times M_{\text{flow}} \dots 4 \times M_{\text{flow}} - 1 \end{cases} \tag{39}$$

where  $U_j^{nms}$ ,  $s=0,1,2,3$ , are the Fourier transforms of the fields formed by the symmetries defined above in (28).

### 3. FORMULATION OF THE GIESEKUS MODEL AND DESCRIPTION OF THE DIRECT SIMULATIONS

The exploration of the dynamics and physics underlying the turbulent flow of dilute polymeric solutions has seen renewed interest in the last decade. This has been principally due to a desire to understand more fully the phenomenon of drag reduction in these flows, otherwise known as the Toms effect [26]. Significant progress has been made in this area due to the development of accurate and efficient numerical algorithms [27], and also to the development of first-principles micromechanical models for polymeric solutions [14, 15]. In general, models which are valid for dilute solutions such as the FENE-P (Finitely extensible non-linear elastic Peterlin) model have been used in the past [28–31]. It was determined in those works that the most crucial viscoelastic property that appears to be responsible for drag reduction is the increased resistance to extensional deformation provided by the polymer molecules. A measure of that increased resistance is the extensional viscosity ratio which, for the FENE-P model, increases from its Newtonian value (of 3) to a limiting value proportional to  $L^2$ , where  $L$  is the molecular extensibility parameter [15].

Here, we have gone a step further and have employed the Giesekus model [32], which has the capability of modelling non-dilute solutions by accommodating concentration effects through the assumption of an anisotropic mobility,  $\alpha$  [14, 15]. When  $\alpha=0$  the anisotropy disappears, while the largest physically meaningful value for that parameter is 1, with typical values ranging from very close to zero (for dilute and semi-dilute polymer systems) to 0.15 for concentrated solutions and melts [15]. In comparison to the FENE-P results, it is interesting to note here that the extensional viscosity ratio for the Giesekus model also increases with increasing extensional rate in extensional flows, with the upper limit being proportional to  $1/\alpha$ . Thus, one can match the extensional viscosity ratios of the Giesekus model to that of the FENE-P by simply adjusting the  $\alpha$  and  $L$  parameters. We use the standard form of the Giesekus model which assumes an infinite polymer extensibility. It can therefore be considered a limiting case of the more general model, the FENE-P/Giesekus model [33], the other limit being the FENE-P model which corresponds to finite extensibility but isotropic mobility. By performing the KL analysis on the Giesekus model with  $\alpha=1/900$ , which is a small value suitable for semi-dilute solutions, we can directly compare our results against previous results based on FENE-P data with  $L=30$  since both of these models correspond to the same extensional viscosity ratio. We note in passing that the Giesekus model has been the model of choice for describing surfactant micellar solutions under drag reducing conditions in turbulent channel flow [34, 35].

Previous results using the Giesekus model in drag reduced turbulent flows [29, 34, 35] have shown modest but measurable changes compared to the FENE-P model: the drag reduction is significantly higher and there are corresponding differences in the turbulence statistics which are compatible with a more drag reducing fluid. Given the interest in modelling more highly drag reducing fluids and in understanding the details of the underlying turbulence in such system we offer here a KL analysis of such flows for the first time. We describe below the application of the MOS to data sets obtained through DNS of drag reduced turbulence using

the Giesekus model and, for comparison, a Newtonian case. We first give a brief description of the equations which embody the Giesekus model and the numerical methods that have been employed in performing the simulations.

A Cartesian  $(x, y, z)$  frame of reference is used. The corresponding velocity components  $(u, v, w)$  are made non-dimensional with  $u^* = \sqrt{(Fh/\rho)}$  where  $F$  is a pressure gradient driving the flow in the streamwise direction,  $h$  is the channel half-width, and  $\rho$  is the density of the solution. In these simulations, the pressure gradient is fixed (independent of time) so that the mass flux (or volume average velocity) is allowed to vary in time. The spatial coordinates and time are non-dimensionalized using  $h$  and  $h/u^*$ , respectively. The pressure,  $p$ , is made non-dimensional using  $\rho u^{*2}$  whereas the extra stress,  $\mathbf{S}$ , due to the polymer is non-dimensionalized using  $\eta_p u^*/h$ , where  $\eta_p$  is the zero shear-rate polymer viscosity.

Using the above non-dimensionalization, the equations governing the motion of the fluid are given by

$$\frac{\partial \mathbf{v}}{\partial t} + \mathbf{v} \cdot \nabla \mathbf{v} = -\nabla p + \frac{\beta_0}{Re} \nabla^2 \mathbf{v} + \frac{1 - \beta_0}{Re} \nabla \cdot \mathbf{S} + \hat{e}_x \quad (40)$$

$$\frac{\partial \mathbf{S}}{\partial t} + \mathbf{v} \cdot \nabla \mathbf{S} - \mathbf{S} \cdot \nabla \mathbf{v} - (\nabla \mathbf{v})^T \cdot \mathbf{S} = \frac{1}{We} (-\mathbf{S} + \boldsymbol{\Sigma}) - \alpha \mathbf{S} \cdot \mathbf{S} + \frac{D}{Re} \nabla^2 \mathbf{S} \quad (41)$$

$$\nabla \cdot \mathbf{v} = 0 \quad (42)$$

where (40) is the momentum equation, (41) is the polymer stress evolution equation, (42) is the continuity equation, and a superscript  $T$  signifies transpose. In these equations  $\mathbf{v} = (u, v, w)$  is the velocity,  $\beta_0$  is the ratio of the solvent viscosity,  $\eta_s$ , to the total (solution) zero shear-rate viscosity,  $\eta_s + \eta_p$ . Additionally,  $\nu = (\eta_s + \eta_p)/\rho$  is the zero shear-rate kinematic viscosity of the solution,  $Re = u^* h/\nu$  is the Reynolds number,  $We = \lambda u^*/h$  is the Weissenberg number where  $\lambda$  is the polymer relaxation time,  $\boldsymbol{\Sigma} = \nabla \mathbf{v} + (\nabla \mathbf{v})^T$  is the shear-rate tensor,  $\hat{e}_x$  is a unit vector in the  $x$  direction which acts as a constant driving pressure,  $\alpha$  is the mobility, and  $D$  is a diffusivity. The importance and efficacy of including the term involving the diffusivity in the evolution equation for the polymer stress has been discussed in detail in Reference [27] and will not be further discussed here.

In the present work, direct numerical simulations of one Newtonian and three viscoelastic cases have been performed. Given the complexity of the problem to be solved, it is very important to minimize all possible reasons that can distort the DNS results. Therefore, special attention is given to the spatial resolution of the computational grid, and the computational domain size ( $L_x$  and  $L_z$ ). The chosen numerical values of these parameters are justified by Housiadas and Beris [27], where a detailed discussion can be found. Briefly, we have chosen a computational grid resolution which lies at the borderline between low accuracy and highly time-consuming simulations. In addition, the computational domain size has to be big enough to allow the largest structures of the flow to develop (viscoelastic structures are larger than the Newtonian ones). We have also been careful to insure that the flow has reached a statistically steady state in all simulations reported here.

The simulation conditions are as follows. For all cases a zero shear-rate friction Reynolds number of 180 has been chosen, the computational box size is  $9 \times 2 \times 4.5$  in the  $x$ ,  $y$ , and  $z$  directions, respectively, and the mesh resolution is  $96 \times 97 \times 96$  in those directions. The non-linear terms in (40) and (41) were fully dealiased in the  $x$ - $z$  plane using a  $144 \times 97 \times 144$  grid according to the standard three-halves rule. The total integration time required to achieve

a statistically steady state is 60 computational units for the Newtonian case, and 80 computational time units for the viscoelastic cases. The rheological conditions are:  $\beta_0 = 0.9$  and  $\alpha = 1/900$  while the numerical diffusion parameter is  $D = 3.25$ . As mentioned above, the value for  $\alpha$  was chosen so as to enable the simulation of a semi-dilute system that exhibits the same extensional resistance as a fluid modelled with a FENE-P model with  $L = 30$ , thus enabling comparisons with previous results [12]. The effect of viscoelasticity on the flow is studied by increasing the Weissenberg number from zero in the Newtonian case to 25, 50, and 125 in the three viscoelastic cases.

## 4. RESULTS

### 4.1. Turbulence statistics

The statistics for the turbulence were obtained from 50 statistically independent realizations in each case. Representative statistics are given in Figures 1–3. The purpose here is to present a sample of the statistics for the Giesekus model though our interest is not to go into detail regarding the interpretation of these results. Such extensive interpretations have been made elsewhere for the Newtonian case [36] and in References [28–31] for the FENE-P model. As we note below, the results for the Giesekus model show trends which are quite similar to those found for the FENE-P model. On the other hand, it is important to point out that the Giesekus model predicts a non-zero (negative) second normal stress difference which is

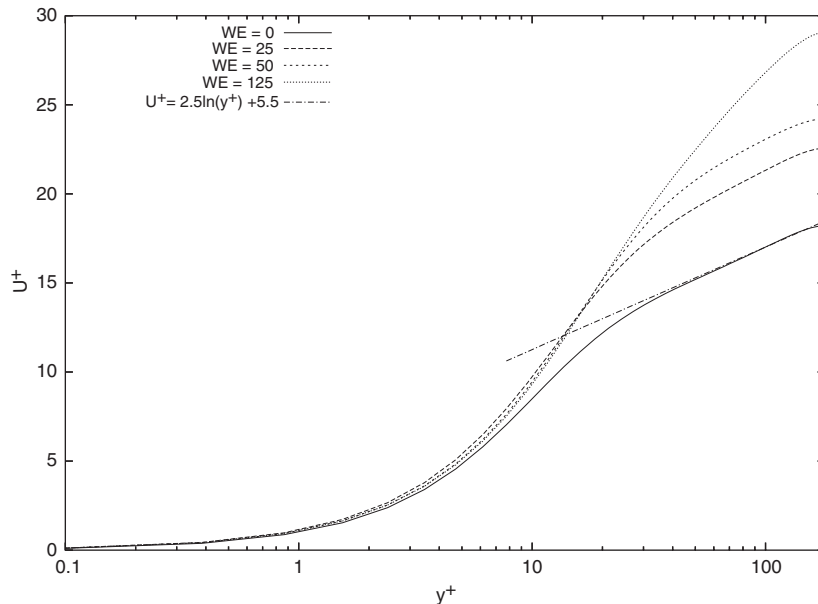


Figure 1. Mean streamwise velocity profiles where  $U^+$  is the mean streamwise velocity made non-dimensional with  $u^*$ , and  $y^+ = yh/\nu$ .

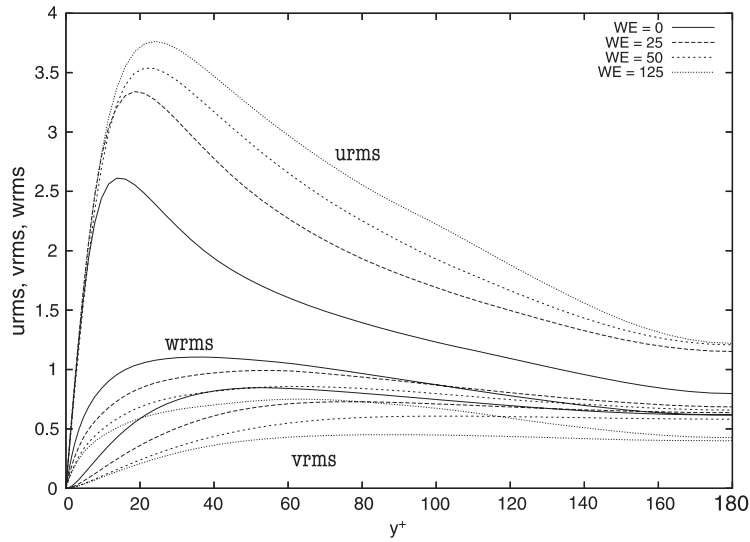


Figure 2. Rms profiles for the streamwise ( $u_{rms}$ ), wall-normal ( $v_{rms}$ ), and spanwise ( $w_{rms}$ ) components of the velocity made non-dimensional by  $u^*$ .

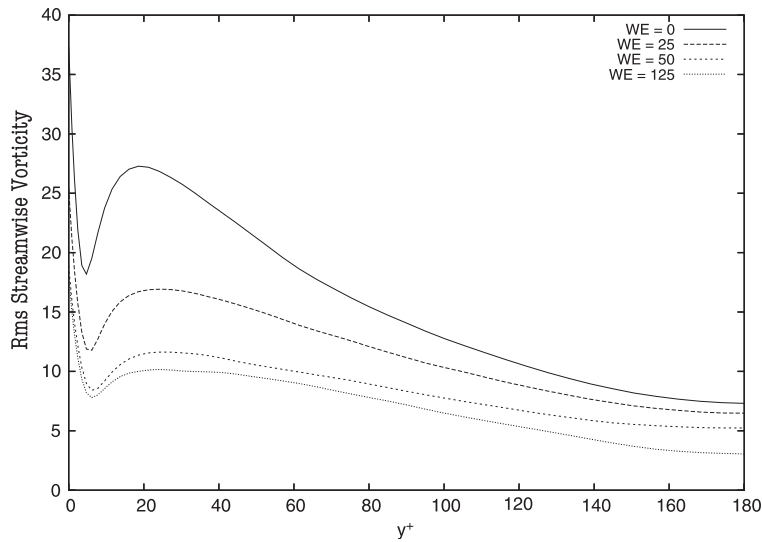


Figure 3. Rms streamwise vorticity profiles made non-dimensional by  $u^*$  and  $h$ .

in contrast to the FENE-P model which predicts no second normal stress difference. Negative second normal stress differences have been associated in the past with enhancement of flow instabilities [37, 38]. We attribute to those differences the modest, but sizeable differences in

turbulence properties (compared to the FENE-P model) that we have mentioned in Section 3 above.

In Figure 1 the mean velocity profiles are shown using standard wall variable scaling. For the Newtonian case ( $We = 0$ ), the velocity profile behaves according to the standard logarithmic law of the wall as expected. The bulk Reynolds number,  $Re_b = U_b h/\nu$ , where  $U_b$  is the bulk (or volume average) velocity, is 2808 and the centreline Reynolds number,  $Re_{cl} = U_{cl} h/\nu$ , where  $U_{cl}$  is the centreline velocity, is 3278. This is in good agreement with the results of Dean [39] which are  $Re_b = 2771$ , and  $Re_{cl} = 3209$ . In the viscoelastic cases, it is evident that the mass flux increases as the Weissenberg number increases with the bulk Reynolds numbers being 3497, 3748, and 4273 for  $We = 25$ , 50, and 125, respectively. The corresponding drag reduction values are 23, 38, and 58% which were obtained using the relations derived by Housiadas and Beris [40].

The root square (rms) profiles for the three components of velocity are given in Figure 2. It is evident, as in the previous work cited above involving the FENE-P model, that as  $We$  increases the rms intensity maxima for each component move farther from the wall, the magnitude of the peak for the rms value of  $u$  increases, and the spanwise and vertical rms values are suppressed. In Figure 3, the rms profiles for the streamwise component of vorticity are given. Again, as shown in previous work with the FENE-P model, the streamwise vorticity fluctuations are significantly decreased in amplitude with their maxima moving farther from the wall as the Weissenberg number increases. Since the streamwise vorticity profiles have been interpreted as indicating the presence of streamwise oriented vortices [41–43], these statistics are clearly indicative of a suppression of the strength and also an increase in the vertical extent of these characteristic flow structures.

#### 4.2. Karhunen–Loeve results for drag reduced turbulence using a Giesekus model

We have applied the MOS as described in Section 2.4 to the turbulent data sets described above. Here we define  $\lambda_I$ ,  $I = 1, 2, 3, \dots$  as the eigenvalue sequence ranked in decreasing order regardless of the values of  $n$ ,  $m$  or  $q$ . In computing the energies associated with each eigenvalue, we have taken into account the degeneracies associated with the reality and symmetries of the flow (see Reference [12]). In the present case we concentrate on the first  $10^4$  eigenvalues, though the calculations yield a total of  $\approx 4 \times 10^5$  eigenvalues. The spectrum of the eigenvalues is shown in Figure 4, starting with the second most energetic eigenvalue,  $\lambda_2$ . The most energetic eigenvalue,  $\lambda_1$ , corresponds to an eigenfunction which represents the mean profile for the streamwise velocity component thereby leaving all other modes to represent deviations from the mean. The spectra shown in Figure 4 clearly indicate that for the Giesekus model, as  $We$  increases, the energy for the lowest modes (say  $I < 200$ ) increases. The opposite is true for the highest modes where increased  $We$  results in a decrease in energy. We also include the curve  $I^{-11/9}$ , which has been shown (see Reference [44]) to represent the inertial subrange in Newtonian turbulence. These results bear some similarity to those exhibited by turbulent channel flow using the FENE-P model [12, 13]. More specifically, we see the very significant strengthening of the low wavenumber eigenmodes and the relative weakening of the higher wavenumber ones, indicating a strengthening of the coherent structures that is generic, independent of the details of the viscoelastic model used, provided that the same essential physics is captured, as, for example, through the matching of the extensional viscosity and the Weissenberg numbers. On the other hand, some peculiarities in the previous

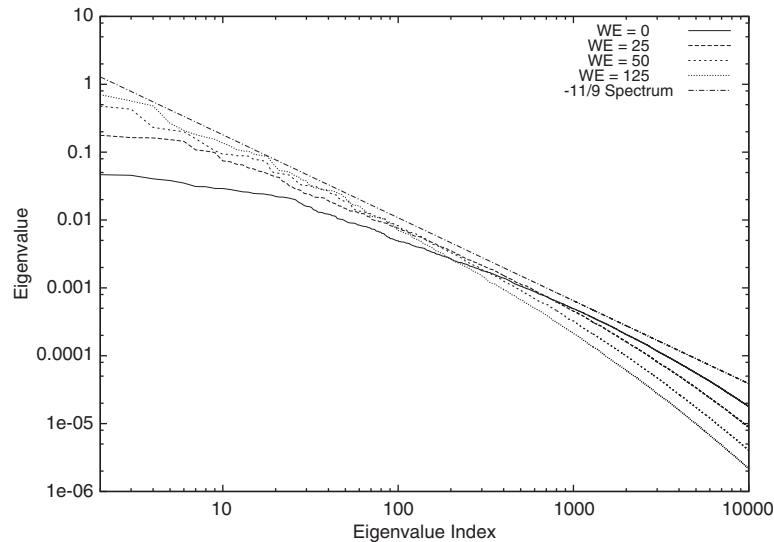


Figure 4. Eigenvalue spectra over a range of Weissenberg numbers for the Giesekus model.

KL results [12], such as a sudden decrease in the eigenvalue magnitude after the seventh eigenvalue, are not seen here indicating possibly that the dropoff was a model-dependent secondary effect.

In Appendix A, we list in Tables AI–AIV, the 15 most energetic modes for each Weissenberg number. For each triplet  $(n, m, q)$  we list the eigenvalues, and the energy fraction  $F_I = \lambda_I/E$ , where  $E = \sum_{I=2}^{N_e} \lambda_I$ , and  $N_e$  is the total number of eigenvalues. We also list the cumulative energy sum  $S_J$ ,  $J = 1, 2, \dots$  where  $S_J = \sum_{I=2}^{J+1} F_I$ . The tables reveal that the most energetic modes tend to be those with little streamwise dependence (e.g.  $n=0$  or 1). Modes with  $n=0$  have been referred to as *roll* modes [3, 4] since they essentially represent infinitely long counter-rotating vortices, while those modes with streamwise dependence are referred to as *propagating* since they may be associated with wave-like behaviour. These modes have also been shown to be associated with the so-called hairpin, or streamwise oriented eddies [5] that have been found in wall-bounded turbulence.

In Figure 5 we plot the so-called KL dimension of the flow, defined as that modal number for which the cumulative energy sum reaches 90%. Thus, when the KL dimension is low, the flow can be considered more *ordered* than a flow with higher dimension since any given amount of flow energy is distributed over fewer modes. It is evident from Figure 5 that the KL dimension decreases more than an order of magnitude from 4730 at  $We=0$  to 268 at  $We=125$ , with the most rapid decrease occurring from  $We=0$  to  $We=50$ . In this range, the KL dimension appears to decrease nearly exponentially as exhibited by the almost linear decrease of dimension number with  $We$  on the semi-log plot of Figure 5.

Lastly we present, in Figures 6–9, both the eigenfunctions and their physical space representations for the most energetic modes in the case  $We=0$  and for the case of highest viscoelasticity,  $We=125$ . In each of these cases the most energetic modes are the so-called

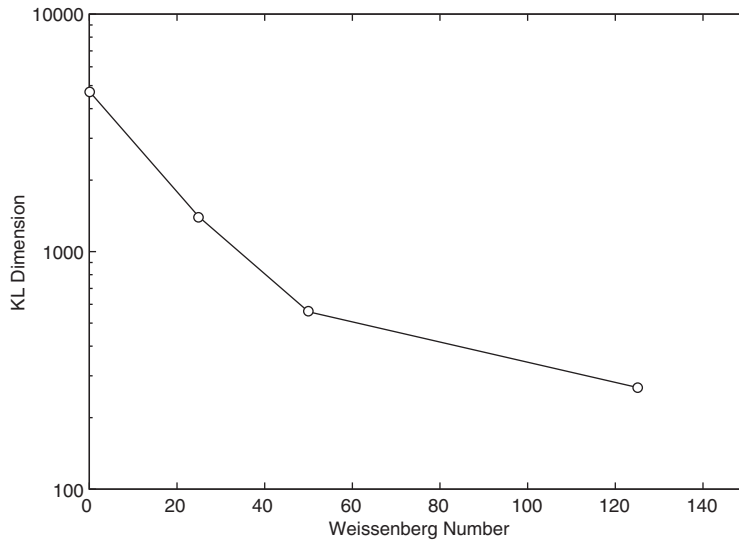


Figure 5. Dependence of KL dimension on Weissenberg number for the Giesekus model.

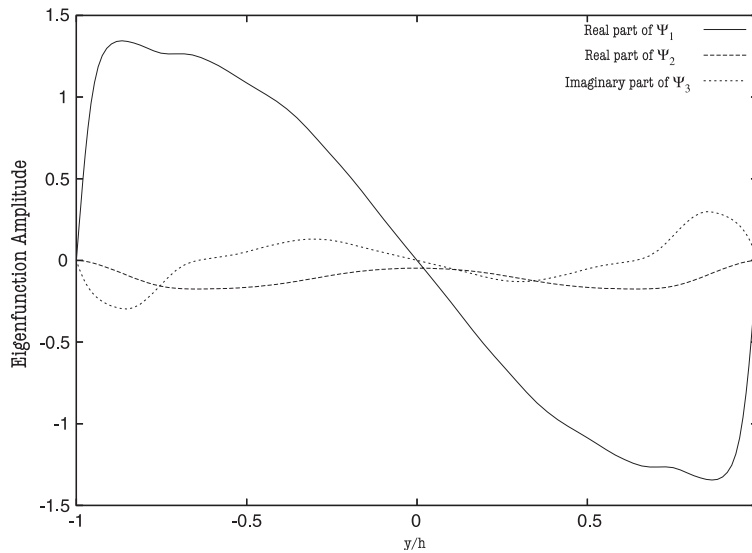


Figure 6. The eigenfunction for  $(n, m, q) = (0, 2, 1)$  for the Newtonian case ( $We = 0$ ).

roll modes as can be seen by referring to the tables in Appendix A. The eigenfunctions for  $We = 0$  for  $(n, m, q) = (0, 2, 1)$  which contains about 1.3% of the energy, and for  $We = 125$  for  $(n, m, q) = (0, 1, 1)$  which contains 10.6% of the energy, are shown in Figures 6 and 7,

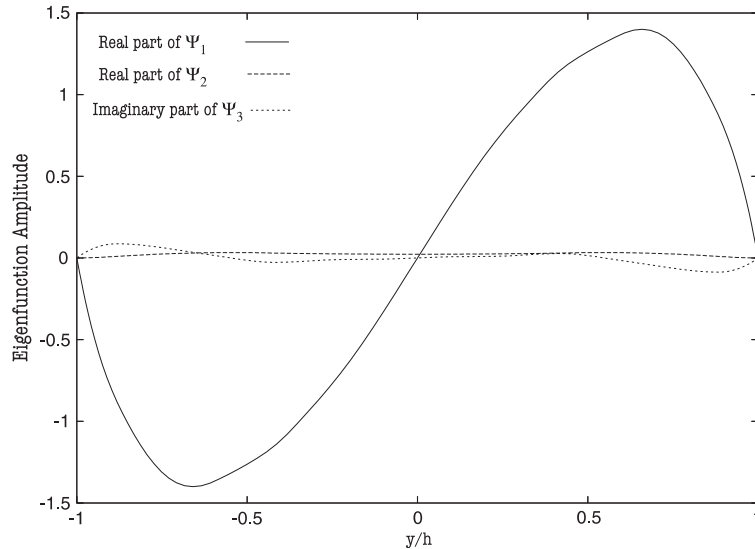


Figure 7. The eigenfunction for  $(n, m, q) = (0, 1, 1)$  for  $(We = 125)$ .

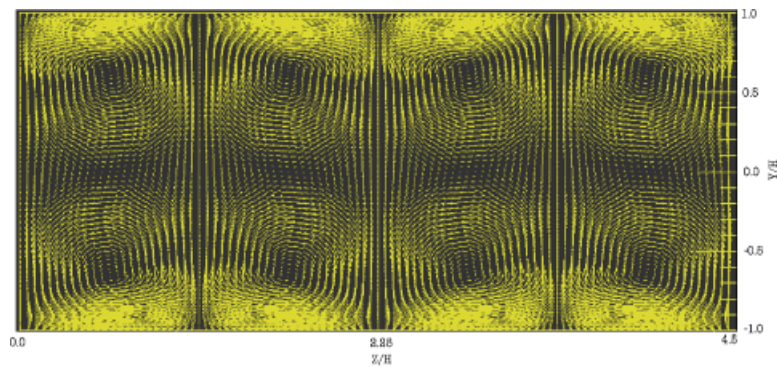


Figure 8. The vector field for the eigenfunction for  $(n, m, q) = (0, 2, 1)$  for the Newtonian case  $(We = 0)$  in the  $z$ - $y$  plane.

respectively. In these figures we need show only the real part of the streamwise and vertical velocity components of the eigenmodes and the imaginary part of the spanwise velocity components since, as shown in Appendix B, in cases for which  $n = 0$ , such a decomposition can be made. These results show quite clearly that for  $We = 125$ , the streamwise component for the  $(0, 1, 1)$  eigenmode peaks significantly farther from the wall compared to the streamwise component of the  $(0, 2, 1)$  mode for  $We = 0$ . In addition, the vertical and spanwise components are noticeably suppressed in amplitude compared to the streamwise component in the  $We = 125$

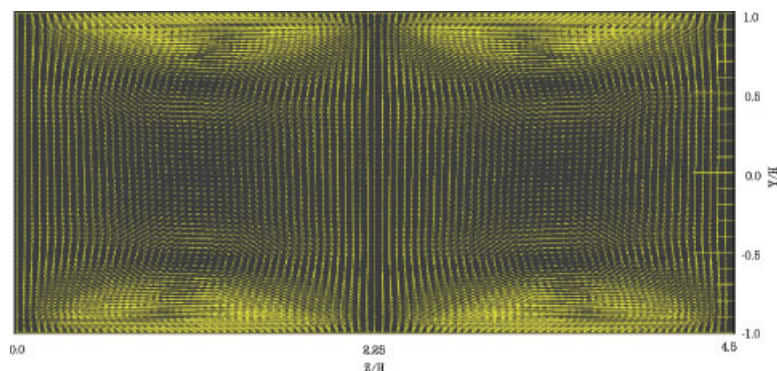


Figure 9. The vector field for the eigenfunction for  $(n, m, q) = (0, 1, 1)$  for  $We = 125$  in the  $z$ - $y$  plane.

case. These two trends are clearly reflected in the overall statistics for both flows as shown above. In addition, we show the vector fields for these eigenmodes  $(\Phi_1(y, z), \Phi_2(y, z), \Phi_3(y, z))$  (see Appendix B) in the  $z$ - $y$  plane in Figures 8 and 9.

In each case, it is clear that these eigenmodes represent counter-rotating vortices (two pairs in the  $(0, 2, 1)$  case and one pair in the  $(0, 1, 1)$  case) and that the vortices in the  $We = 125$  case are significantly larger in their vertical extent than those for  $We = 0$ . We note that although these modes lack streamwise dependence, they are fully three-dimensional in the sense that all three velocity components are non-zero. Therefore, due to the existence of a streamwise velocity component, the particle paths associated with these vortices can be shown to be helical in nature. These results confirm the general view of viscoelastic turbulence which is that it consists of larger more energetic scales compared to their Newtonian counterparts at the same Reynolds number.

## 5. SUMMARY AND CONCLUSIONS

The KL method has recently been used extensively to describe and interpret complex three-dimensional turbulent flows, and to construct low-order models for these flows. The standard method for performing the analysis, the so-called direct method (DM), typically involves solving a spatial eigenvalue problem on non-uniform grids. Here we have shown that the problem can be easily reformulated in terms of a temporal eigenvalue problem using the so-called method of snapshots (MOS).

It is shown that the MOS, although it is mathematically equivalent to the DM, affords some computational advantages. First, the correlation matrix  $C^{nm}$  in the MOS has purely scalar components compared to the tensor nature of  $R_{ij}$  needed for the DM. More importantly, the weight functions, which are required in the DM, are completely avoided in the MOS. These facts have two main consequences: (1) The construction of  $C^{nm}$  does not require the assembly of a matrix of matrices as in the DM, and (2) In the MOS no issues arise as to the singularity of the weight functions at the boundaries. In the MOS, since weights are entirely avoided in the construction of  $C^{nm}$ , any boundary conditions satisfied by the flow will be automatically

preserved in the eigenfunctions. It is also straightforward to incorporate the flow symmetries discussed above into the MOS. It is hoped that the MOS as formulated here will be considered in some cases as a useful alternative to the direct approach.

We have applied the three-dimensional version of the MOS to the case of viscoelastic turbulence described by a Giesekus model, which has the capability to describe non-dilute systems. The results reveal that strong viscoelasticity reduces the dimensionality of the turbulence by more than an order of magnitude. The energy in the largest turbulent scales are substantially enhanced at the expense of the smaller dissipative scales. These trends were quite similar to the results obtained earlier using a FENE-P model, although here we were able to perform a KL analysis for the case ( $We = 125$ ) in which the drag reduction was large (58%). We have shown features that are generic to viscoelastic turbulent flows (the substantial strengthening of the low wavenumber modes and a significant decreased dimensionality) and have therefore shown the usefulness of performing such KL analyses using the MOS method described above. Moreover, we have also looked at the spatial structure of the dominant eigenmodes in both the Newtonian case and in the case of the highest Weissenberg number. These modes turn out to be those with no streamwise variation. The results show that the modes in the viscoelastic case describe counter-rotating streamwise oriented vortices with more energetic (relative to the Newtonian case) streamwise velocity fluctuations and less energetic wall-normal and spanwise velocity fluctuations.

## APPENDIX A

Tables (Tables AI–AIV) for the 15 most energetic Karhunen–Loeve modes for  $We = 0, 25, 50, 125$ .

Table AI. First 15 KL modes for  $Re = 180$  and  $We = 0$  (Newtonian case). Definitions of the energy fraction and energy sum are given in Section 4.2. Index 1 represents the most energetic eigenmode, excluding the  $(0, 0, 1)$  mode which represents the mean flow.

Index	$\lambda$	$n$	$m$	$q$	Energy fraction	Energy sum
1	0.46571E – 01	0	2	1	0.13120E – 01	0.13120E – 01
2	0.45501E – 01	0	3	1	0.12819E – 01	0.25939E – 01
3	0.40425E – 01	1	3	1	0.11389E – 01	0.37328E – 01
4	0.38242E – 01	1	2	1	0.10774E – 01	0.48102E – 01
5	0.34965E – 01	1	4	1	0.98507E – 02	0.57953E – 01
6	0.31186E – 01	0	2	2	0.87859E – 02	0.66739E – 01
7	0.30995E – 01	0	4	1	0.87320E – 02	0.75471E – 01
8	0.29167E – 01	1	4	2	0.82171E – 02	0.83688E – 01
9	0.29105E – 01	1	1	1	0.81998E – 02	0.91888E – 01
10	0.28136E – 01	1	3	2	0.79268E – 02	0.99814E – 01
11	0.27082E – 01	0	3	2	0.76299E – 02	0.10744E + 00
12	0.25975E – 01	1	2	2	0.73179E – 02	0.11476E + 00
13	0.25746E – 01	0	1	1	0.72533E – 02	0.12202E + 00
14	0.24663E – 01	0	5	1	0.69481E – 02	0.12896E + 00
15	0.24335E – 01	1	6	1	0.68559E – 02	0.13582E + 00

Table AII. First 15 KL modes for  $Re = 180$  and  $We = 25$  (Giesekus model). Definitions of the energy fraction and energy sum are given in Section 4.2. Index 1 represents the most energetic eigenmode, excluding the  $(0, 0, 1)$  mode which represents the mean flow.

Index	$\lambda$	$n$	$m$	$q$	Energy fraction	Energy sum
1	0.17726E + 00	0	1	1	0.35140E - 01	0.35140E - 01
2	0.16373E + 00	0	1	2	0.32457E - 01	0.67597E - 01
3	0.16199E + 00	0	3	1	0.32113E - 01	0.99710E - 01
4	0.15290E + 00	0	2	1	0.30311E - 01	0.13002E + 00
5	0.14425E + 00	0	4	1	0.28596E - 01	0.15862E + 00
6	0.10797E + 00	0	3	2	0.21404E - 01	0.18002E + 00
7	0.10360E + 00	0	2	2	0.20538E - 01	0.20056E + 00
8	0.98583E - 01	0	4	2	0.19543E - 01	0.22010E + 00
9	0.74207E - 01	1	3	1	0.14711E - 01	0.23481E + 00
10	0.72315E - 01	0	5	1	0.14336E - 01	0.24915E + 00
11	0.66167E - 01	1	2	1	0.13117E - 01	0.26227E + 00
12	0.64748E - 01	1	1	1	0.12835E - 01	0.27510E + 00
13	0.58511E - 01	1	2	2	0.11599E - 01	0.28670E + 00
14	0.56570E - 01	0	5	2	0.11214E - 01	0.29791E + 00
15	0.52762E - 01	1	1	2	0.10459E - 01	0.30837E + 00

Table AIII. First 15 KL modes for  $Re = 180$  and  $We = 50$  (Giesekus model). Definitions of the energy fraction and energy sum are given in Section 4.2. Index 1 represents the most energetic eigenmode, excluding the  $(0, 0, 1)$  mode which represents the mean flow.

Index	$\lambda$	$n$	$m$	$q$	Energy fraction	Energy sum
1	0.47441E + 00	0	1	1	0.79770E - 01	0.79770E - 01
2	0.42989E + 00	0	2	1	0.72284E - 01	0.15205E + 00
3	0.23130E + 00	0	3	1	0.38893E - 01	0.19095E + 00
4	0.21227E + 00	0	3	2	0.35692E - 01	0.22664E + 00
5	0.19946E + 00	0	2	2	0.33539E - 01	0.26018E + 00
6	0.15793E + 00	0	1	2	0.26555E - 01	0.28673E + 00
7	0.12692E + 00	0	4	1	0.21341E - 01	0.30807E + 00
8	0.10527E + 00	0	4	2	0.17701E - 01	0.32578E + 00
9	0.92898E - 01	0	1	3	0.15620E - 01	0.34140E + 00
10	0.92736E - 01	1	2	1	0.15593E - 01	0.35699E + 00
11	0.88440E - 01	1	3	1	0.14871E - 01	0.37186E + 00
12	0.88389E - 01	0	5	1	0.14862E - 01	0.38672E + 00
13	0.86999E - 01	1	1	1	0.14629E - 01	0.40135E + 00
14	0.78246E - 01	1	1	2	0.13157E - 01	0.41451E + 00
15	0.76832E - 01	1	2	2	0.12919E - 01	0.42743E + 00

APPENDIX B: PHYSICAL SPACE REPRESENTATION OF THE EIGENFUNCTIONS FOR WHICH  $n = 0$

We define the physical space representation of the eigenfunctions,  $\Phi_j(y, z)$ , for which there is no streamwise dependence ( $n = 0$ ) by

$$\Phi_j(y, z) = \Psi_j^{(0, m, q)}(y) e^{ik_m z} + \Psi_j^{(0, -m, q)}(y) e^{-ik_m z} \tag{B1}$$

Table AIV. Eigenvalues for first 15 KL modes for  $Re = 180$  and  $We = 125$  (Giesekus model). Definitions of the energy fraction and energy sum are given in Section 4.2. Index 1 represents the most energetic eigenmode, excluding the  $(0,0,1)$  mode which represents the mean flow.

Index	$\lambda$	$n$	$m$	$q$	Energy fraction	Energy sum
1	0.70320E + 00	0	1	1	0.10597E + 00	0.10597E + 00
2	0.56677E + 00	0	3	1	0.85406E - 01	0.19137E + 00
3	0.48032E + 00	0	2	1	0.72379E - 01	0.26375E + 00
4	0.26682E + 00	0	2	2	0.40208E - 01	0.30396E + 00
5	0.20963E + 00	0	0	2	0.31589E - 01	0.33555E + 00
6	0.18085E + 00	0	4	1	0.27253E - 01	0.36280E + 00
7	0.16580E + 00	0	3	2	0.24985E - 01	0.38778E + 00
8	0.15458E + 00	1	2	1	0.23294E - 01	0.41108E + 00
9	0.13646E + 00	0	0	3	0.20563E - 01	0.43164E + 00
10	0.12297E + 00	0	1	2	0.18530E - 01	0.45017E + 00
11	0.10906E + 00	0	5	1	0.16434E - 01	0.46660E + 00
12	0.10365E + 00	0	1	3	0.15618E - 01	0.48222E + 00
13	0.10324E + 00	1	2	2	0.15558E - 01	0.49778E + 00
14	0.93881E - 01	1	1	1	0.14147E - 01	0.51193E + 00
15	0.90418E - 01	1	3	1	0.13625E - 01	0.52555E + 00

where  $\Psi_j^{(0,m,q)}$  are the Karhunen–Loeve eigenfunctions evaluated for  $n=0$ . Since the original eigenfunctions  $\Psi_j^{n,m,q}$  have been computed from real data and since a spanwise reflectional symmetry has been imposed via (28) it can easily be shown that the eigenfunctions satisfy:

$$\Psi_j^{(0,m,q)} = \overline{\Psi_j^{(0,-m,q)}}, \quad j = 1, 2, 3 \tag{B2}$$

and

$$\begin{aligned} \Psi_1^{(0,m,q)} &= \Psi_1^{(0,-m,q)} \\ \Psi_2^{(0,m,q)} &= \Psi_2^{(0,-m,q)} \\ \Psi_3^{(0,m,q)} &= -\Psi_3^{(0,-m,q)} \end{aligned} \tag{B3}$$

where the dependence on  $y$  is suppressed in (B2) and (B3). It follows from (B2) and (B3) that  $\Psi_1^{(0,m,q)}$  and  $\Psi_2^{(0,m,q)}$  are real and  $\Psi_3^{(0,m,q)}$  is imaginary, and that therefore the physical space representation of the eigenfunctions with  $n=0$  can be written using (B1) as

$$\begin{aligned} \Phi_1(y, z) &= 2 \times \text{RE}[\Psi_1^{(0,m,q)}(y)] \cos(k_m z) \\ \Phi_2(y, z) &= 2 \times \text{RE}[\Psi_2^{(0,m,q)}(y)] \cos(k_m z) \\ \Phi_3(y, z) &= -2 \times \text{IM}[\Psi_3^{(0,m,q)}(y)] \sin(k_m z) \end{aligned} \tag{B4}$$

ACKNOWLEDGEMENTS

The authors would like to acknowledge the financial support provided by DARPA, Grant No. MDA972-01-1-0007. We are grateful to the National Center for Supercomputing Applications (NCSA) for pro-

viding the extensive computational resources needed for this work through an Alliance proposal grant under Grant No. MCA96N005P. We also acknowledge the computational resources provided by the DOD High Performance Computing (HPC) program.

## REFERENCES

1. Preisendorfer RW. *Principal Component Analysis in Meteorology and Oceanography*. Elsevier: New York, 1988.
2. Moin P, Moser RD. Characteristic eddy decomposition of turbulence in a channel. *Journal of Fluid Mechanics* 1989; **200**:471–509.
3. Sirovich L, Ball KS, Keefe LR. Plane waves and structures in turbulent channel flow. *Physics of Fluids A* 1990; **2**:2217–2226.
4. Sirovich L, Ball KS, Handler RA. Propagating structures in wall bounded turbulent flow. *Theoretical and Computational Fluid Dynamics* 1991; **2**:307–317.
5. Webber GA, Handler RA, Sirovich L. The Karhunen–Loeve decomposition of minimal channel flow. *Physics of Fluids* 1997; **9**:1054–1066.
6. Aubry N, Holmes P, Lumley JL, Stone E. The dynamics of coherent structures in the wall region of a turbulent boundary layer. *Journal of Fluid Mechanics* 1988; **192**:115–173.
7. Zhou X, Sirovich L. Coherence and chaos in a model of the turbulent boundary layer. *Physics of Fluids A* 1992; **4**:2855–2874.
8. Sirovich L, Xhou X. Dynamical model of wall bounded turbulence. *Physical Review Letters* 1994; **72**:340–343.
9. Webber GA, Handler RA, Sirovich L. Energy dynamics in a turbulent channel flow using the Karhunen–Loeve approach. *International Journal for Numerical Methods in Fluids* 2002; **40**:1381–1400.
10. Sirovich L. Turbulence and the dynamics of coherent structures. *Quarterly Journal of Applied Mathematics* 1987; **45**:561–590.
11. Sirovich L, Kirby M. Low dimensional characterization of human faces. *Journal of the Optical Society of America* 1987; **4**:519–524.
12. Housiadas KD, Beris AN, Handler RA. Viscoelastic effects on higher order statistics and on coherent structures in turbulent channel flow. *Physics of Fluids* 2005; **17**:035106.
13. De Angelis E, Casciola CM, L'vov VS, Piva R, Procaccia I. Drag reduction by polymers in turbulent channel flows: energy redistribution between invariant empirical modes. *Physical Review E* 2003; **67**:056312.
14. Tanner RI. *Engineering Rheology*. Oxford University Press: New York, 2000.
15. Bird RB, Armstrong RC, Hassager O. *Dynamics of Polymeric Liquids*, vols. 1–2. Wiley: New York, 1977.
16. Cannuto C, Hussaini MY, Quarteroni A, Zang TA. *Spectral Methods in Fluid Dynamics*. Springer: New York, 1987.
17. Lam K, Banerjee S. On the condition of streak formation in a bounded turbulent flow. *Physics of Fluids A* 1992; **4**:306–326.
18. Handler RA, Swean TF, Leighton RI, Swearingen JD. Length scales and the energy-balance for turbulence near a free-surface. *AIAA Journal* 1993; **31**:1998–2007.
19. Nagaosa R, Handler RA. Statistical analysis of coherent vortices near a free surface in a fully developed turbulence. *Physics of Fluids* 2003; **15**:375–394.
20. Handler RA, Saylor JR, Leighton RI, Rovelstad AL. Transport of a passive scalar at a shear-free boundary in fully developed turbulent open channel flow. *Physics of Fluids* 1999; **11**:2607–2625.
21. Sarpkaya T. Vorticity, free surfaces, and surfactants. *Annual Review of Fluid Mechanics* 1996; **28**:83–128.
22. Smith GB, Volino RJ, Handler RA, Leighton RI. The thermal signature of a vortex pair impacting a free surface. *Journal of Fluid Mechanics* 2001; **444**:49–78.
23. Handler RA, Leighton RI, Smith GB, Nagaosa R. Surfactant effects on passive scalar transport in a fully developed turbulent flow. *International Journal of Heat and Mass Transfer* 2003; **46**:2219–2238.
24. Batchelor GK. *An Introduction to Fluid Mechanics*. Cambridge University Press: New York, 1967.
25. Lumley JL. *Stochastic Tools in Turbulence*. Academic: New York, 1970.
26. Toms BA. Some observations on the flow of linear polymer solutions through straight tubes at large Reynolds numbers. *Proceedings of the International Congress on Rheology*, vol. 2. North Holland: Amsterdam, 1949; 135–141.
27. Housiadas KD, Beris AN. An efficient fully implicit spectral scheme for DNS of turbulent viscoelastic channel flow. *Journal of Non-Newtonian Fluid Mechanics* 2004; **122**:243–262.
28. Sureshkumar R, Beris AN, Handler RA. Direct numerical simulation of the turbulent channel flow of a polymer solution. *Physics of Fluids* 1997; **9**:743–755.
29. Dimitropoulos CD, Sureshkumar R, Beris AN. Direct numerical simulation of viscoelastic turbulent channel flow exhibiting drag reduction: effect of the variation of rheological parameters. *Journal of Non-Newtonian Fluid Mechanics* 1998; **79**:433–468.

30. Dimitropoulos CD, Sureshkumar R, Beris AN, Handler RA. Budgets of Reynolds stress, kinetic energy, and streamwise enstrophy in viscoelastic turbulent channel flow. *Physics of Fluids* 2001; **13**:1016–1027.
31. Housiadas KD, Beris AN. Polymer-induced drag reduction: effects of the variations in elasticity and inertia in turbulent viscoelastic channel flow. *Physics of Fluids* 2003; **15**:2369–2384.
32. Giesekus H. A simple constitutive equation for polymer fluids based on the concept of deformation-dependent tensorial mobility. *Journal of Non-Newtonian Fluid Mechanics* 1982; **11**:69–109.
33. Housiadas KD, Beris AN. DNS of turbulent viscoelastic channel flow for a finite extension, semi-dilute polymer system. 2005, in press.
34. Yu B, Kawaguchi Y. Effect of Weissenberg number on the flow structures: DNS study of drag reducing flow with surfactant additives. *International Journal of Heat and Fluid Flow* 2003; **24**:491–499.
35. Yu B, Li FC, Kawaguchi Y. Numerical and experimental investigation of turbulent characteristics in a drag reducing flow with surfactant additives. *International Journal of Heat and Fluid Flow* 2004; **25**:961–974.
36. Kim J, Moin P, Moser R. Turbulence statistics in fully-developed channel flow at low Reynolds number. *Journal of Fluid Mechanics* 1987; **177**:133–166.
37. Renardy YY, Renardy M. Instability due to second normal stress jump in two-layer shear flow of the Giesekus fluid. *Journal of Non-Newtonian Fluid Mechanics* 1999; **81**:215–234.
38. Renardy M. On the mechanism of drag reduction. *Journal of Non-Newtonian Fluid Mechanics* 1995; **59**:93–101.
39. Dean RB. Reynolds number dependence of skin friction and other bulk flow variables in two dimensional rectangular duct flow. *Journal of Fluids Engineering—Transactions of the ASME* 1978; **100**:215–223.
40. Housiadas KD, Beris AN. Characteristic scales and drag reduction evaluation in turbulent channel flow of non-constant viscosity viscoelastic fluids. *Physics of Fluids* 2004; **16**:1581–1586.
41. Robinson SK. Coherent motions in the turbulent boundary layer. *Annual Review of Fluid Mechanics* 1991; **23**:601–639.
42. Brooke JW, Hanratty TJ. Origin of turbulence producing eddies in a channel flow. *Physics of Fluids A* 1993; **5**:1011–1022.
43. Bernard PS, Thomas JT, Handler RA. Vortex dynamics and the production of Reynolds stress. *Journal of Fluid Mechanics* 1993; **253**:385–419.
44. Knight B, Sirovich L. Kolmogorov inertial range for inhomogeneous turbulent flows. *Physical Review Letters* 1990; **65**:1356–1359.